Applied Energy 252 (2019) 113421

Contents lists available at ScienceDirect

Applied Energy

journal homepage: www.elsevier.com/locate/apenergy

Spatially resolved oxygen reaction, water, and temperature distribution: Experimental results as a function of flow field and implications for polymer electrolyte fuel cell operation

Thiago Lopes[a,d,e,*], Otavio Beruski[b,d], Amit M. Manthanwar[c,1], Ivan Korkischko[d,e], Reynaldo Pugliesi[d], Marco Antonio Stanojev[d], Marcos Leandro Garcia Andrade[d], Efstratios N. Pistikopoulos[c,1], Joelma Perez[b], Fabio Coral Fonseca[d], Julio Romano Meneghini[e], Anthony R. Kucernak[a,*]

[a] *Department of Chemistry, Imperial College London, South Kensington Campus, London SW7 2AZ, United Kingdom*
[b] *Instituto de Quimica de Sao Carlos, Universidade de Sao Paulo, Sao Carlos 13566-590, Sao Paulo, Brazil*
[c] *Department of Chemical Engineering, Imperial College London, London SW7 2AZ, United Kingdom*
[d] *Nuclear and Energy Research Institute, IPEN/CNEN-SP, Sao Paulo-SP 05508-000, Brazil*
[e] *Research Centre for Gas Innovation, University of Sao Paulo, Escola Politecnica, Ave Prof Mello Moraes 2231, Sao Paulo-SP 05508030, Brazil*

HIGHLIGHTS

- In situ and ex situ spatially-resolved techniques.
- Reactant distribution impacts in a polymer electrolyte fuel cell.
- Contribution of convection in heat as well as reactant distribution.
- Water build-up from neutron tomography is linked to component degradation.
- Local current densities might shape degradation patterns in fuel cells.

GRAPHICAL ABSTRACT

A multi-technique approach towards understanding the impacts of fluid flow on fuel cells.

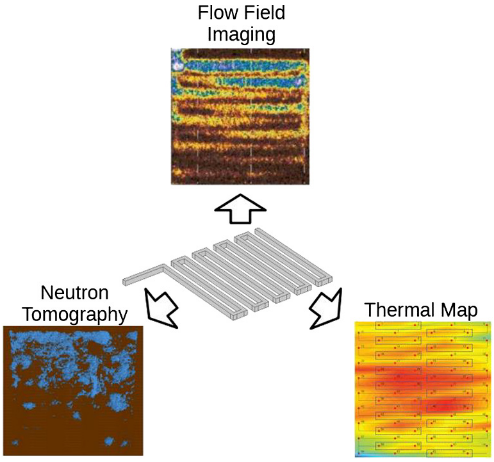

ARTICLE INFO

Keywords:
Fuel cell
Catalyst layer utilization
Oxygen imaging
Temperature mapping

ABSTRACT

In situ and ex situ spatially-resolved techniques are employed to investigate reactant distribution and its impacts in a polymer electrolyte fuel cell. Temperature distribution data provides further evidence for secondary flows inferred from reactant imaging data, highlighting the contribution of convection in heat as well as reactant distribution. Water build-up from neutron tomography is linked to component degradation, matching the pattern

---

[*] Corresponding authors at: Nuclear and Energy Research Institute, IPEN/CNEN-SP, Sao Paulo-SP 05508-000, Brazil (T. Lopes), Department of Chemistry, Imperial College London, UK (A. Kucernak).

E-mail addresses: thiago_lopes@usp.br (T. Lopes), anthony@imperial.ac.uk (A.R. Kucernak).

[1] Present address: Texas A&M Energy Institute, College Station, United States.

https://doi.org/10.1016/j.apenergy.2019.113421
Received 19 February 2019; Received in revised form 27 May 2019; Accepted 31 May 2019
0306-2619/

Neutron tomography

seen in the reactant distribution and thus suggesting that high, non-uniform local current densities shape degradation patterns in fuel cells. The correlations shown between different techniques confirm the use of the versatile reactant imaging technique, which is used to compare commonly used flow field designs. Among serpentine-type designs, the single serpentine is superior in both equivalent current density and reactant distribution, showing large contributions from convective flow. On the other hand, the interdigitated design is shown to produce larger equivalent current densities, while showing a somewhat poorer reactant distribution. Considering the correlations drawn between the techniques, this suggests that the interdigitated design compromises durability in favour of power output. The results highlight how established techniques provide a robust background for the use of a new and flexible imaging technique toward designing advanced flow fields for practical fuel cell applications.

1. Introduction

Flow fields, a network of interconnected microchannels, are the lungs of fuel cell systems. They are vital towards both longevity and reliability of these systems, especially for low temperature devices at an industrial scale [1]. This is reflected in the number of work exploring innovative flow field designs, such as Baik and Seo [2], Huo et al. [3] and Li et al. [4], as well as studies of cell management, for instance those collected and explored by Borup et al. [5] and, more recently, that of Ashrafi and Shams [6]. Fuel cells are envisioned to be a pillar of a sustainable society [7–9], however uneven reactant distribution across fuel cell electrodes which impacts efficiency, durability and reliability is still a matter of ongoing research [1,2,4,10]. Wang and Wang [11–13] have pointed out that uneven flow distribution is the main cause of degradation of fuel cells after scaling up. However, this has not been accepted widely in the fuel cell community. It is still an open issue for discussion and debate for a variety of reasons: (i) the outward appearances of failures are materials, water and thermal (hotspots) issues; (ii) the need for improved in situ techniques to map the inhomogeneity of species and heat distribution along the catalyst layer area at high resolutions; and (iii) advanced models validated by such in situ techniques.

In the early 1990's, Watkins et al. [14,15] showed a 50% increase in a fuel cell power output level just through appropriate distribution of reactants. More recently, for high temperature fuel cells, Dey et al. [16] obtained a 100% increase in cell performance by changing the anode channels from a mesh to a straight design. A recent example of flow field design promoting low temperature fuel cell performance is that of the Toyota MIRAI car, where a 3D mesh flow field type has promoted a 2.4 times increase in cell current density (this value also includes improvements of the oxygen reduction reaction catalyst) [17]. These findings suggest that, species distribution through fuel cell layers is an important step towards understanding and improving fuel cell performance, durability and reliability, since it enables us to understand and optimize the flux of reactants and heat distribution through each cell component with experimentally validated advanced computational models [18]. Therefore, in situ techniques which enables a high-resolution detection of species and heat distribution through fuel cell layers are of paramount importance towards practical applications of such devices.

Some in situ techniques have been developed over the years to characterize polymer electrolyte fuel cells (PEFCs), as can be seen in references [5,19,20]. The most relevant examples, in the context of species and temperature distribution, are highlighted below. Measurement of the oxygen concentration along the cathode channel of a PEFC may be accomplished by fluorophore molecules sensitive to quenching by oxygen, [21]. However, this technique provides relatively low temporal and spatial resolutions, of 500 ms and 300 μm, respectively. Recently, an optical technique has been recently developed to overcome these issues [22]. The tool is based on a chemiluminescent reaction, which emits light at a high intensity and allows high spatial resolutions to be achieved (< 20 μm). This method is employed in the present work to image, in situ, the flow pattern and to measure the local concentration of reactant at the cathode catalyst layer of a pseudo-PEFC.

Temperature distribution on PEFCs presents a high spatial heterogeneity, being intrinsically coupled to the flow dynamics, affected by parameters such as the flow rate [23] and flow field design [2,24]. There are some techniques available to map the temperature distribution on the surface of PEFC electrodes (see for instance reference [25] and references therein). Among the in situ techniques, it could be argued that thermocouples render high spatial and temporal resolutions at high accuracy (0.3 °C), if properly designed [26–28]. This technique is utilized in the present work to map the temperature at the surface of both anode and cathode electrodes of a PEFC *in operando*, providing in situ evidence of the impact of the species distribution on the temperature distribution.

Direct visualization of water in a PEFC is of paramount importance for improving performance and durability of this important technology, while boosting model validation [29]. A number of techniques have been developed, including X-ray radiography [30,31] and tomography [32], NMR imaging [33,34] and neutron scattering [35], radiography [36–38] and tomography [39], where the latter allows reconstruction of a three dimensional view of the water content in the membrane and electrode assembly (MEA). This technique is explored in the present work to gain insights on the impact of fluid flow dynamics on the durability of PEFCs.

This brief literature review highlights the great importance of in situ characterization tools in guiding a rational understanding of the performance, durability and reliability of PEFCs, since uneven reactant distribution at the catalyst layer may lead to local temperature increases and local electrolyte dehydration, while reactant deprivation leads to higher overpotential and possibly corrosion of the catalyst support [29]. An uneven heat distribution can potentially lead to uneven proton transport resistances across the MEA [40–42]. This in turn can lead to increased Joule heat generation through both the membrane and the catalyst layer, resulting in further local dehydration. This cascading effect may lead to the formation of hotspots, which in turn may lead to system failure. With this in mind we aim to provide insights into the impact of species distribution on PEFC systems though in-situ techniques, suitably employed in order to draw correlations between the different phenomena involved. The insights provided from these techniques are then applied to commonly used prototype flow field designs, in order to improve the understanding on what drives performance and durability in each one. We hope that by using a flexible and relatively easy-to-use technique, under the guidance of validated computational models and well established experimental techniques, it will be possible to create a framework where flow field designs are routinely conceptualized, created and tested, improving our understanding and optimising FC performance and durability. Towards achieving such goals, the remainder of this work is organized as follows. Section 2 describes the materials and hardware used, as well as the experimental techniques employed: reactant imaging, in situ temperature distribution, and neutron tomography. Section 3 presents the results, drawing correlations between the different techniques; later further exploring the reactant imaging technique for different flow field designs. Section 4 summarizes and concludes this work, pointing out the impact of reactant distribution in practical PEFC devices and the need to further develop and validate both computational and experimental techniques towards tackling this issue.

2. Experimental

2.1. Electrodes and MEA preparation

Three different electrode structures were used to help understand reactant transport within the fuel cell structure.

Type A electrodes were commercial Johnson Matthey platinum-catalyst based electrodes, at a platinum loading of 0.4 mg_{Pt}/cm^2, purchased from Alfa Aesar (hydrogen electrode/reformate cathode, 50 cm^2), and utilised a Toray carbon paper as porous transport layer (PTL). To prepare the membrane electrode assemblies (MEAs), two 50 cm^2 type A electrodes and a Nafion NR212 membrane were hot-pressed at 135 °C under a load of 50 kg cm^{-2} for three minutes. Type A electrodes were utilised to map the temperature profile along the respective MEAs of a PEFC under operation with type A hardware.

Type B electrodes were designed to mimic the performance of real fuel cell electrodes (but were not fuel cell electrodes in themselves) and were composed of materials which allowed the oxygen partial pressure (as ozone) to be followed as a function of position within the electrode structure. The catalyst layers were prepared in a similar way to chemiluminescent ozone sensors described in the literature [43], in which 7-diethylamino-4-methylcoumarin (coumarin 1, Sigma Aldrich, 99%) is deposited on nanosilica gel (nanosilica gel on TLC plates, Sigma Aldrich) along with gallic acid, where the later acts as energy transfer agent and the former as light emitting reagent in the presence of ozone. This modified (or pseudo) “catalyst layer” was sandwiched between a Toray TGP-H-60 carbon paper porous transport layer (PTL) and a glass plate (see below). The overall reaction is proposed to proceed via the Forster-resonant energy transfer mechanism [22], where the energy transfer reactant reacts with ozone to produce a product in an excited state, and then the excess energy is transferred to the coumarin dye, which luminesces. A detailed description of the sensor preparation and optimization procedure is given in a published paper [22]. As Type B electrodes were not electrochemically active the systems utilising these electrodes used a glass plate, which replaces the polymer electrolyte membrane in an actual PEFC. Such configuration allowed visualisation of the pseudo “catalyst layer” within which the light producing reactions occur. Type B electrodes were utilised to map the reactant partial pressure profile along the pseudo PEFC with type B hardware.

Type C electrodes were prepared as per type A electrodes, though the membrane was a Nafion™ N115 and the cathode catalyst was a carbon-based catalyst of the type FeN_x/C [44] at a loading of 4 mg_{cat} cm^{-2}, which resulted in a catalyst layer thickness of 130 μm [45,46]. The carbon-based catalyst was synthesized and deposited on a Toray carbon paper (with microporous layer) as described in references [45,47]. Type C electrodes were utilised to image the water profile along the MEAs of a post-operation PEFC (further details are given in Section 2.5).

2.2. Fuel cell hardware

Three different types of fuel cell hardware were used. The first was used to measure the performance of real fuel cell electrodes within a

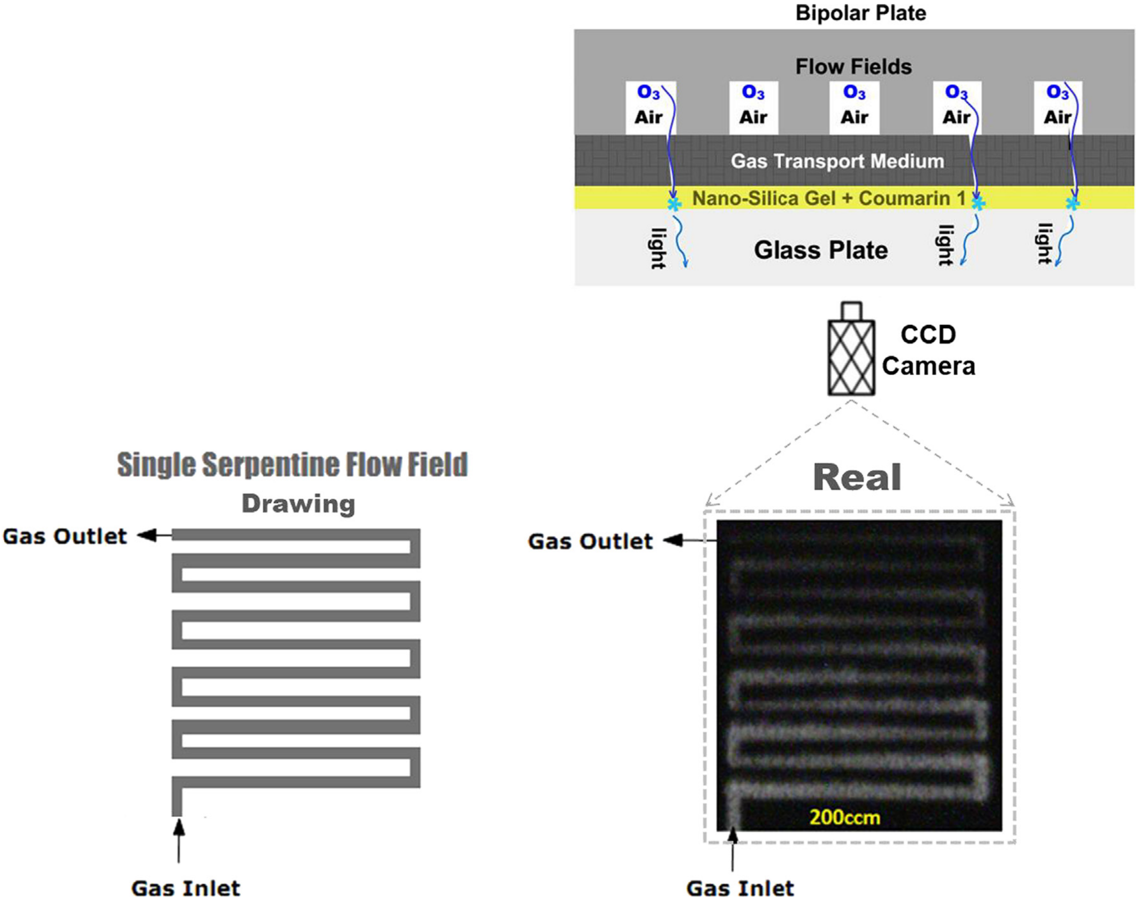

Fig. 1. Schematic of the indirect oxygen imaging system. The top cartoon illustrates the flow pattern of oxygen (as ozone) across the catalyst layer of a pseudo PEFC. The gas stream flows through a single serpentine flow field channel, where it is subsequently transported through an actual PEFC transport medium (carbon paper, Toray TGP-H-60) before reaching the catalyst layer. The gas is an enriched ozone (~1230 ppm) air stream, at a flow rate of 200 ccm, at room temperature (~25 °C).

typical operating environment, the second was used to mimic those conditions within an operating fuel cell and the third was used to prepare a real fuel cell MEA for neutron tomography measurements (details of this hardware are given in Section 2.5).

Type A hardware, for MEA temperature mapping, was custom made by Fuel Cell Technologies, Inc. Briefly, a 12.7 mm thick resin impregnated POCO industrial grade AXF-5Q graphite block, had single serpentine flow fields machined to a width of ~2 mm (0.078 in.) and a depth of ~1.6 mm (0.062 in.). A gold plated current collecting metal sheet (~2.5 mm thick) were placed between the graphite block and an electrically insulated temperature controlling metal block (~30 mm thick). Type E thermocouples (Omega Engineering), with an experimentally determined accuracy of ± 0.25 °C (95% confidence interval) [28], were placed within the flow field channels to touch the surface of the PTL of the MEA. Along the flow field length, an array of 64 thermocouples were placed on the anode and 64 on the cathode, a diagram of the measurement system, data acquisition and communication apparatus, is given in another publication [28].

Type B hardware, for reactant imaging, was constructed out of glass-reinforced epoxy laminate sheets (FR4), which were precisely machined with a CNC machine (Bungard CCD/ATC) to an equivalent fuel cell active area of 5 cm^2, though with various flow field designs. FR4 boards were chosen due to its advantages over graphite blocks, for instance, inertness to ozone (and a general inertness) [22], ease of machining and design, and being cheaper and simpler to work with. The various flow field designs studied in this work are given in supplementary material Figure S1, namely, single, double, triple serpentine, and interdigitated. These designs were chosen in order to analyse the development of gas flux within fuel cell components, and to better understand the impact of convective flow to oxygen partial pressure distribution within the catalyst layer.

2.3. Light measurement during chemiluminescence

A controlled flow rate of air (mass flow controller FMA 3706, Omega Engineering Limited) was passed through a suitable ozone generator (BMT Sesstechnik, Berlin, Germany, model: BMT-801) in order to produce an ozone enriched (1230 ppm) air stream of constant concentration (quantification occurred at the known ozone UV absorption peak, $\lambda_{max} = 253.7$; $\varepsilon = 3000 \pm 30\,dm^3\,mol^{-1}\,cm^{-1}$ [48], for further experimental details refer to [22]). This ozone enriched air stream was directed to the above described fuel cell replica. Upon flowing through the fuel cell flow fields, the ozone enriched air stream is transported towards the catalyst layer through the porous media. Within the catalyst layer, it reaches the light emitting dye. The light generated from the reaction between ozone and the coumarin-based dye was recorded with a CCD camera (Abus WDR 3D DNR Day/Night 650 TVL) utilising a Sony Super HAD CCDIIsensor, which provides an appropriate low light performance and a linear response. The setup is enclosed in a light-sealed box, with an experimental diagram displayed in [22]. As illustrated in Fig. 1, the flow dynamics of the ozone through the fuel cell flow field and microporous layer to reach the catalyst layer is recorded with the CCD camera to generate a video. The fuel cell membrane is mimicked here by a glass sheet (Fig. 1), making it possible to visualize the flow dynamics of the oxygen at the important catalyst layer of the fuel cell. It is appropriate to note that the interaction of ozone with the components of the pseudo PEFC have been carefully analysed elsewhere [22], using an on-line UV–Vis and a mass spectrometer. It was shown that at room temperature ozone only reacts with the dye and does not react with cell components, even at increased levels of ~20,000 ppm of ozone.

The videos recorded of the chemiluminescent reaction between ozone and the coumarin-based dye at the catalyst layer of the fuel cell replica allows quantification of ozone concentration (i.e. the local oxygen partial pressure) and the spatial distribution of oxygen (as ozone). The former quantification is possible given the optimisation of the ozone detection method described in Ref. [22]. Frames of the videos recorded were analysed with the public domain Java image processing program, ImageJ [49]. This suitable software allows for appropriate image manipulation, for instance construction of histograms, consistent subtraction of backgrounds etc.

2.4. In situ temperature measurement

Type A electrode and type A hardware were utilised to map the temperature profile along the surface of the porous transport layer of a 50 cm^2 PEFC under operation. A fuel cell test station from Scribner Associates Inc. (model 850e) was used to perform the tests. The anode compartment was fed with pure hydrogen (99.999%, BOC UK Ltd) and the cathode with pure air at a fixed flow rate of 1.1 $L\ min^{-1}$ and 4.5 $L\ min^{-1}$ respectively, equivalent to a stoichiometry of 1.5 and 2.5 at a current density of 1.66 $A\ cm^{-2}$. During PEFC tests, the cell hardware was maintained at 80 °C and humidification water bottle temperatures were maintained at 80 °C (80 °C dew points). The PEFC was conditioned at 0.6 V for two hours and subsequently VI (polarisation) curves were carried out until reproducible curves were obtained (between two to three curves were usually performed), prior to constant potential measurements – with concomitant MEA temperature measurements. A description of the temperature measurement apparatus and procedure is given in Section 2.2 and in Ref. [28].

2.5. Neutron tomography measurement

A 5 cm^2 single serpentine channel fuel cell hardware from Fuel Cell Technologies Inc. was utilised for experiments aimed to measure the water distribution at the cathode electrode of a post-operation MEA. The as prepared MEA was assembled to the fuel cell hardware and connected to a fuel cell test station from Fuel Cell Technologies Inc. The anode compartment was fed with pure hydrogen (99.999%) and the cathode with pure oxygen (99.99%) at a fixed flow rate of 160 $mL\,min^{-1}$ and of 550 $mL\,min^{-1}$ respectively. During PEFCs tests, the cell hardware was maintained at 80 °C and humidification water bottles were maintained at 95 $°C_{anode}$ and 85 $°C_{cathode}$. The cell was conditioned for two hours at a current density resulting in cell voltage of about 0.4 V and subsequently four VIR (polarisation) curves (forward-backward scan) were carried out. In sequence, the cell was held for about 30 min at 0.6 V, 0.5 V, 0.4 V, 0.3 V and 0.2 V, and finally two more VI curves were recorded. This MEA was removed from the PEFC hardware and placed in di-ionized (DI) water for ~170 h to equilibrate. This MEA were then vacuum dried for ~170 h and taken to the nuclear reactor at the Nuclear and Energy Research Institute, for neutron imaging tomography experiments. First, a tomography was taken of the dry MEA, which was then equilibrated in water for ~170 h for a second tomography. This procedure was taken aiming at imaging regions of the MEA where water would be retained as a result of intermolecular interactions between water and oxygen functional groups created on the carbon materials of the electrode (gas transport media and catalyst layer). Therefore, the neutron tomography technique was employed to visualize how water is distributed within the MEA. The equipment for tomography is installed at the 5 MW IEA-R1 Nuclear Research Reactor, of the IPEN-CNEN/SP. It consists of a rotating table where the MEA was positioned for irradiation, a scintillator screen where the image of its internal structure is formed, a plane mirror that reflects this image to a digital video camera, where it is recorded. Two software analysis packages were used: one for image reconstruction, which generates the tomography slices in the three planes of view XY, XZ, YZ, and the second for 3D image visualization. For the present equipment the neutron flux at the irradiation position is $8 \times 10^6\,n\,s^{-1}\,cm^{-2}$, the maximal beam diameter is 16 cm, the time required to obtain a data set is 400 s and the thickness of each tomography slice is 0.14 mm [50,51]. These data are presented in Section 3.3 though a 3D neutron view of the water along the MEA, from which a slice-by-slice analysis is presented in Figure S2. Moreover, in order to demonstrate in which part of the MEA the water is more concentrated, all the slices of the tomography, for this same plane of view, were scanned, and the obtained results showed that close to 100% of the occurrences, corresponding to the higher water concentration, are present in the cathode region (electrode and membrane).

3. Results

Recently, a new imaging method based on chemiluminescence to indirectly image oxygen at the catalyst layer of a pseudo PEFC has been developed [22]. It uses an allotrope of dioxygen, ozone, to mimic the passage of oxygen gas through a fuel cell replica. Ozone diluted in air interacts with a coumarin-based dye system resulting in a chemiluminescent reaction. The ozone interacts with the dye similarly to dioxygen and a metal catalyst in a fuel cell cathode, resulting in the emission of photons in the visible range, as depicted in the schematic representation in Fig. 1. Measuring the light emission from this catalyst layer allows determination of the local ozone concentration [22] and hence rate of oxygen reaction, mimicking the behaviour of the local current density in a PEFC cathode. This allows an indirect probe of the flow field in a system very similar to a FC cathode (in the absence of the effects of water flooding). In another work [18], the experimental results reported in [22] have been compared to mathematical models describing the transport of species in such pseudo PEFC cathodes. The validated model confirmed some of the propositions of the experimental work with further insights about the fluid dynamics in PEFCs. As a relevant example of such insights, it was quantitatively shown the importance of convection for improving the power density in practical PEFCs. The initial studies have analysed single serpentine flow field designs, intended to establish and validate the technique as a powerful imaging tool in PEFC research. Here, we broaden the scope and carry out an in-depth analysis on how species transport in a PEFC impacts its performance, correlating different imaging techniques to suggest that flow field design might be as important as, say, the chosen catalyst.

3.1. Species distribution via the reactant imaging technique

Fig. 2 illustrates the reactant partial pressure distribution for a range of inlet flow rates and flow field designs, showing at the uppermost line the single serpentine (SS) flow field. Also shown are the double and triple serpentine configurations (DS and TS, respectively), and the interdigitated flow field (ID). We provide information on the mass flow rate, equivalent average flow speed, and Reynolds number (Re) for a single channel in each of the different situations. The latter two are calculated for a single channel, although the local properties might be different due to the various geometrical and flow effects described below. We also provide the equivalent oxygen stoichiometry (λ – see below). The analysis will first focus on the SS flow field, in order to correlate with the other imaging techniques used. We shall return later (Section 4) to compare between flow fields, using the species distribution surfaces presented in Fig. 2 and the insights provided by the correlation with the temperature distribution (Section 3.2) and neutron tomography (Section 3.3).

Recently, we have shown that the validated computational model strongly suggests that the ozone transport closely reproduces the transport of oxygen in an actual fuel cell [18]. Therefore, the response in Fig. 2 closely represent the distribution of oxygen gas along the

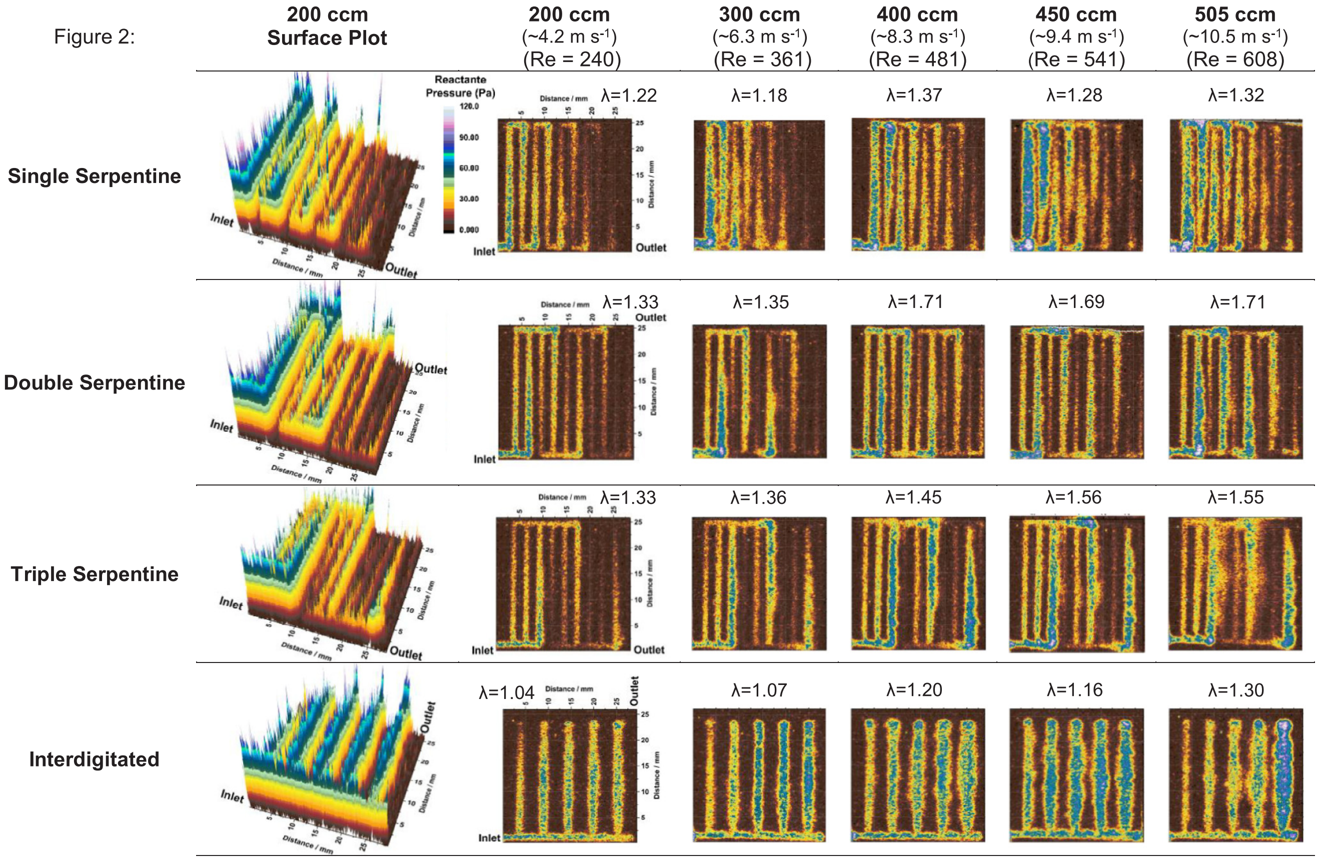

Fig. 2. Images represent the surface and contour plots of the partial pressure distribution of oxygen (as ozone) along the catalyst layer of a pseudo PEFC (5 cm^2 "electrode" area). The partial pressure of reactant results from the flow of gas through a PEFC replica and then through an actual PEFC gas transport medium (carbon paper, Toray TGP-H-60). Images compare the impact of various flow field designs and gas flow rates on the partial pressure magnitude and distribution along the catalyst layer of the practical device replica. The reactive gas is an enriched ozone (~1230 ppm) air stream at room temperature (~25 °C) under different flow rates and measured ozone stoichiometry, as indicated in the figure.

catalyst layer of an actual PEFC. Regions with high mass transport rates are seen as having higher reactant partial pressures due to increased convective fluxes from the flow channel and through the porous transport layer (fuel cell carbon paper). Analysing Fig. 2 shows that the partial pressure of reactant gradually reduces from gas inlet to outlet. This closely replicates the consumption of oxygen along the flow field of an actual *in operando* PEFC via measuring the current distribution along the electrode [52–55] or the actual oxygen concentration decay along the length of the channel [56]. Data presented in Fig. 2 also illustrates that the reactant partial pressure at the catalyst layer is increased upon U turns in the serpentine-type flow fields – there is a decrease in reaction upstream of the U-bend but increased reaction at the downstream side of the U-Bend. This phenomenon was also seen in the computational model [18], being interpreted as a consequence of secondary flow, in the form of vortices, which strongly shape the partial pressure and distribution of reactant gas throughout the catalyst layer and positively impacts PEFC performance. The existence of such vortices has also been measured through laser Doppler anemometry analysis of an in operando PEFC [57]. It is also interesting to note that Yoshizawa et al. have shown that adding obstacles (i.e. manifold and seal) to the flow path in a serpentine configuration causes a substantial improvement in the performance of a PEFC [58] which also suggests the contribution of secondary flow to more effective mass transport of reactant species, in agreement with the present findings. Similar effect was observed in a modelling study [59] on the effect of adding obstacles along the flow field length impacting the PEFC performance, where PEFC performance increased substantially with the number of obstacles (higher fractional contribution of convection to the total fluid flow).

A single-channel serpentine is the most common flow field design for PEFCs of small active electrode area. Some of the features described in the literature [60] for this flow field design are: (i) it would ensure exposure of the entire electrode area to reactive gas; (ii) the fluid velocity would be high enough to push any water condensed in the channel out of the cell; (iii) a pressure drop along the channel would be due to friction of the fluid with the channel walls and transport layer and due to turns; and (iv) pressure differences between adjacent channels would cause bypassing of fluid at portions of the channel. Data in Fig. 2 are of paramount importance to elucidate these listed features and the physical phenomena underlying them. At a suitably high gas flow rate (Fig. 2, rightmost surface, Re = 608), it is seen that the electrode area is not uniformly exposed to the reactive gas: regions under the lands (ribs) and, most remarkably, right before U turns are significantly deprived of reactant. Utilizing neutron radiography, Yoshizawa et al. [58] have shown that, in S-type flow fields, water accumulates at the channel's corners (i.e. U turns) and outside the channel. Based on Fig. 2 and on our recent modelling results [18], vortices arising at U turns might probably be responsible for the accumulation of water at these regions by pushing species away from the gas pathway, thus hindering its transport down the channel. As pointed out earlier, these vortex regions are seen as regions of high reactant partial pressure (e.g. at the second corner of U turns). Mass flux arising from these secondary flows and the pressure drop along the channel can be observed to contribute to the crossover of gas to neighbouring channels. These phenomena expand the area of the electrode accessed by the reactant gas, being quite pronounced right after U turns, and diminishing towards the end of a channel leading to the next U turn. These results suggest that bypassing of gas at portions of the serpentine channel is mostly caused by secondary flow in U turns, which, in turn, might also contribute to water accumulation in the land portions as the magnitude of the flow rate is significantly lower than over the channels. Utilizing neutron imaging, Spendelow et al. [61] and Kowal et al. [62] have shown that, for single serpentine and straight channels, the amount of water in the land region is indeed higher than that in the channel region of an in operando PEFC, which is interestingly seen in both anode and cathode. Through synchrotron X-ray radiography with a spatial resolution of 3 μm, Hartnig et al. [63] have also verified this effect. Therefore, the present findings might inspire ways of tackling water management in PEFCs, since Fig. 2 provides evidence for the reduced presence of reactant under the land area, and as a result of convective flux of species in this region.

3.2. In situ temperature distribution of an in operando PEFC

Practical PEFCs operate close to 0.7 V [64] whereas the thermoneutral potential for these systems is 1.482 V (based on hydrogen's higher heating value). Therefore, more than half of the chemical energy stored in the fuel is converted into heat during the operation of a PEFC, where this generated heat is resultant from entropic heat (difference between the maximum work, ΔG, and the heating value of the fuel) irreversible heat (anode and cathode overpotentials) and Joule heat (resulting from the internal ohmic resistances of the cell). This points to the fact that regions along the MEA with higher concentrations of reactant would also have higher generation of heat (i.e. higher local reaction rate), which would in turn result in regions of higher

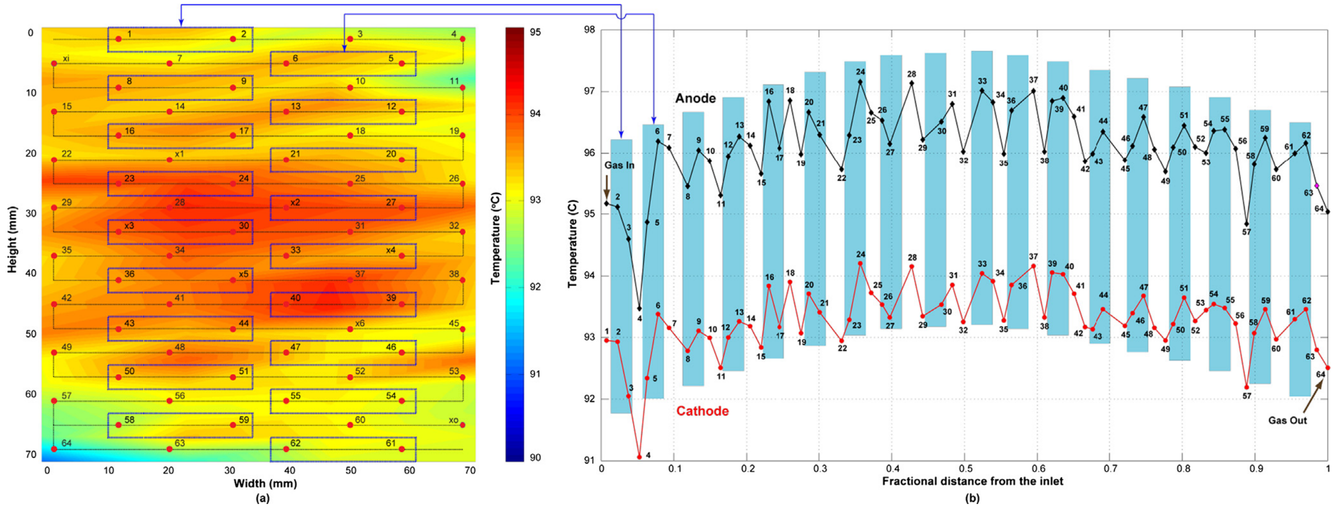

Fig. 3. The temperature distribution image and graph illustrate the temperature distribution at the surface of the macroporous layer (carbon paper) and along the flow field length, respectively, of a PEFC in operando at a fixed voltage of 0.4 V. Experimental details: 50 cm^2 PEFC feed with H_2 (99.999%, BOC)/Air at a flow rate of 1.120 L min^{-1}/4.460 L min^{-1}. PEFC hardware at 80 °C feed with humidified gases at 100 RH%. Backpressure was not applied. A Nafion™ membrane NR212 was utilised as electrolyte membrane and both anode and cathode were the commercial Johnson Matthey platinum electrode at a loading of 0.4 $mg_{Pt}cm^{-2}$.

temperature. Based on data in Fig. 2 for a single serpentine flow field design, regions presenting higher temperatures would be right after U turns and regions with lower temperature would appear right before U turns. Data in Fig. 3 present the temperature distribution along the flow field area for both anode and cathode of a 50 cm^2 PEFC under operating conditions. Fig. 3a shows the locations where the temperatures were measured. Regions immediately after 'U' turns are highlighted with rectangles in both images of the Fig. 3. Data in Fig. 3b show an interesting profile: the temperature along the flow field presents a trend, being higher right after U turns and lower right before, similar to the results seen for the degree of reaction in Fig. 2. These results suggest that managing reactant distribution should be carried out with extreme care in order to generate a most homogeneous distribution of reactant with approximate equal partial pressure along the entire MEA area. As will be shown below, peaks in reactant partial pressure are accompanied by peaks in temperatures, which then result in both heat management and longevity issues for a PEFC. Local temperature increases in a PEFC causes a local dehydration of the proton conducting electrolyte (both in the membrane and catalyst layer), since, for instance, a 5 °C increase in temperature results in a ~17% decrease in the water vapour saturation pressure at an operating temperature of 80 °C. This reduction increases the local ohmic heat generation due to a local increase in ionic resistance, which further dehydrates the polymer electrolyte (both in the membrane and catalyst layer). Such effects negatively impacts both PEFC performance and longevity. Therefore, it is apparent that tackling reactant management would remarkably and positively contribute to improve heat management in PEFCs. This result further highlights the importance of reactant management in practical devices, and how the present reactant imaging technique can suitably promote it.

3.3. Ex situ water accumulation in a post-operando PEFC via neutron tomography

The durability of cathode electrodes has been shown to be intimately related to the presence of oxygen by Borup et al. [5] and Wood et al. [65] These authors exposed a mass transport layer to aging environments, i.e. purging nitrogen or air (O_2) in water at 60 °C or 80 °C for 480–680 h. The results pointed out that the increase in temperature from 60 °C to 80 °C had less an impact on the decrease in contact angle and loss in hydrophobicity than the presence of dissolved oxygen. This is a consequence of the oxidation of carbon structures in the electrode producing oxygenated groups [66,67] which are hydrophilic in nature and thus prone to reduce the contact angle, to retain water and to promote flooding in the cathode electrode [29]. Considering the reactant distribution profiles given in Fig. 2 (and the temperature distribution measurements given below) and the results of Borup et al. [5] and Wood et al. [65], it would appear intuitive that a PEFC electrode would be more susceptible to corrosion in the regions of the catalyst layer with higher reactant partial pressure, where the wetting properties (i.e., hydrophilicity) of the electrode would change the most. It is interesting to note that the reactant profile shown in Fig. 2 is similar to the local current density profile measured by Takanohashi et al. [68], at high reactant utilization levels, such as those use in the present study. The cited literature and data in Figs. 2 and 3 would possibly suggest the existence of a carbon corrosion gradient along the MEA of a PEFC after operation. Such a gradient would be accompanied by a water retention gradient, being higher at the reactant inlet and lower at the outlet, following the reactant partial pressure profile. If this assumption were to be correct, considering the results presented in Fig. 2, the regions close to the oxygen inlet of a PEFC would present a higher concentration of water than the region close to the reactant outlet. To explore this phenomenon, neutron tomography experiments were carried out with a post-operation MEA which had used a carbon-based cathode catalyst. This catalyst was chosen given its emerging importance [44–47,69],

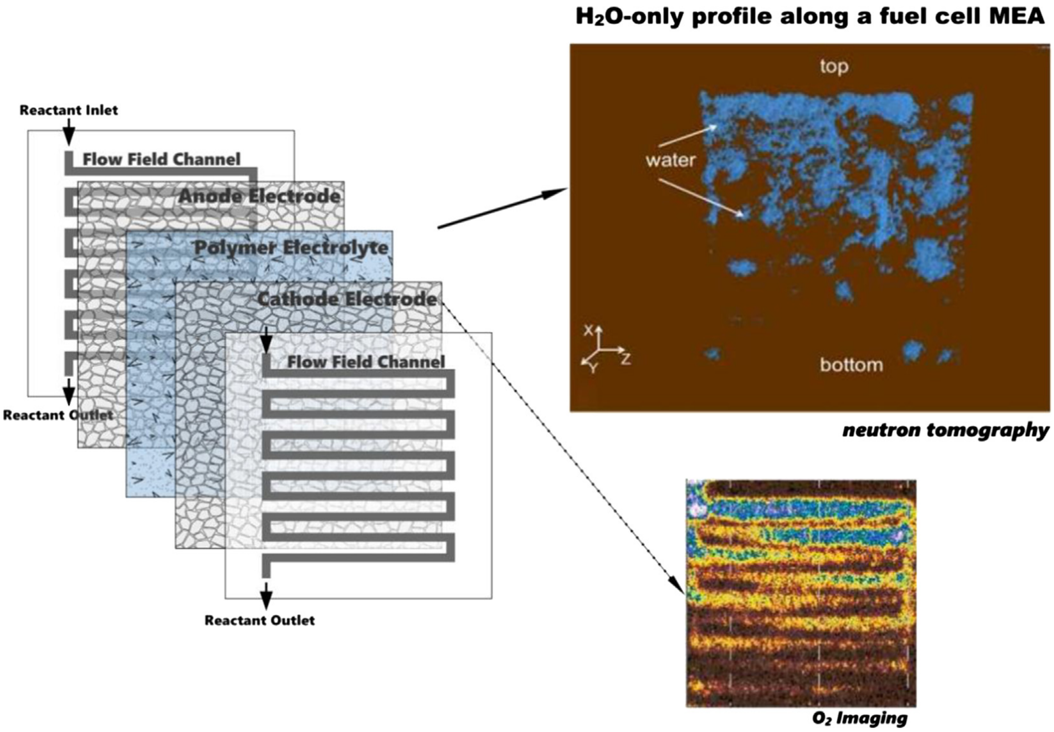

Fig. 4. Neutron imaging illustrates the water gradient distribution along the MEA of a post operation 5 cm^2 polymer electrolyte fuel cell, which was measured ex-situ by neutron tomography. An image of the reactant distribution (O_2 Imaging) along the catalyst layer of a pseudo PEFC (5 cm^2) with identical single serpentine channels is also given for direct comparison (image at 450 ccm given in Fig. 3), as measure by the present indirect oxygen imaging method. The schematic image illustrates the layers of a PEFC for clarity.

and greater sensitivity to corrosion under PEFC conditions, when compared to the carbon black support of state-of-the-art platinum-based catalysts [70,71]. To exclude water dynamics occurring during the operation of a PEFC, this experiment was conducted after cell operation (see experimental section for details), where a tomography of the dry electrode was subtracted from that of the same MEA equilibrated in water for ~170 h. This subtraction would ideally represent only the water retention throughout the MEA resulting from the oxidation of carbon structures (most notably at the cathode). A result of this experiment is presented in Fig. 4 (and S5) where the amount of water as seen by neutron tomography is higher in regions closer to the oxygen inlet, which further suggests that the presented ex situ reactant imaging results are capable of providing information on actual PEFC phenomena. It is noteworthy that water and heat management are different depending on the scale, i.e. when comparing a 5 cm^2 to a 50 cm^2 MEA. Nevertheless, this neutron tomography result further suggests that under operation, the management of reactant partial pressure distribution in the catalyst layer area is crucial considering durability of fuel cells, and that the imaging technique used in this work could guide advancements in PEFC longevity. This points to a scenario where proper distribution of reactants over the electrode area leads to reduced local stress on the catalyst layer and therefore improves durability of fuel cell electrodes and system as a whole. This corroboration and suggestions highlight the potential of the present reactant imaging technique towards developing suitable practical devices.

4. Discussion

Multichannel serpentine flow field configurations were initially proposed in order to reduce the pressure drop of single-channel designs in larger PEFC electrode areas [60]. According to the data in Fig. 2, a higher partial pressure of reactant is observed mainly along one of the channels, where regions of lower reactant partial pressure seem to increase with the number of channels. This effect is clearly observed in the response plots shown in Fig. 2. Multichannel serpentine design, with lower channel flow velocity, are likely to generate a reduced mean local/total current density. Such a decrease has been observed through modelling [72,73], and is attributed to mass transport issues in experimental results [74]. It is noteworthy that, from the experimental results of Tabe et al. [75] and Hwnag et al. [76] for current distribution using a segmented cell approach, it is seen that higher local current densities are seen upon U turns for multiserpentine flow field designs, as also seen in the results in Fig. 2. Considering that liquid water is absent in the experimental setup of Fig. 2, and present in the cited literature [75,76], the convergence of these scenarios suggests that reactant distribution is strongly linked to the flow field design.

An interesting alternative to the S-type design is the interdigitated flow field. In this configuration the channels are discontinuous, that is the inlet and outlet manifolds are not connected. This design forces the fluid to pass from inlet to outlet channels through the porous transport layer. Results in Fig. 2 indirectly provide evidence for this phenomenon, further, and interestingly, showing that reactive gas is mostly seen only in the catalyst layer region underneath the inlet channels. These data

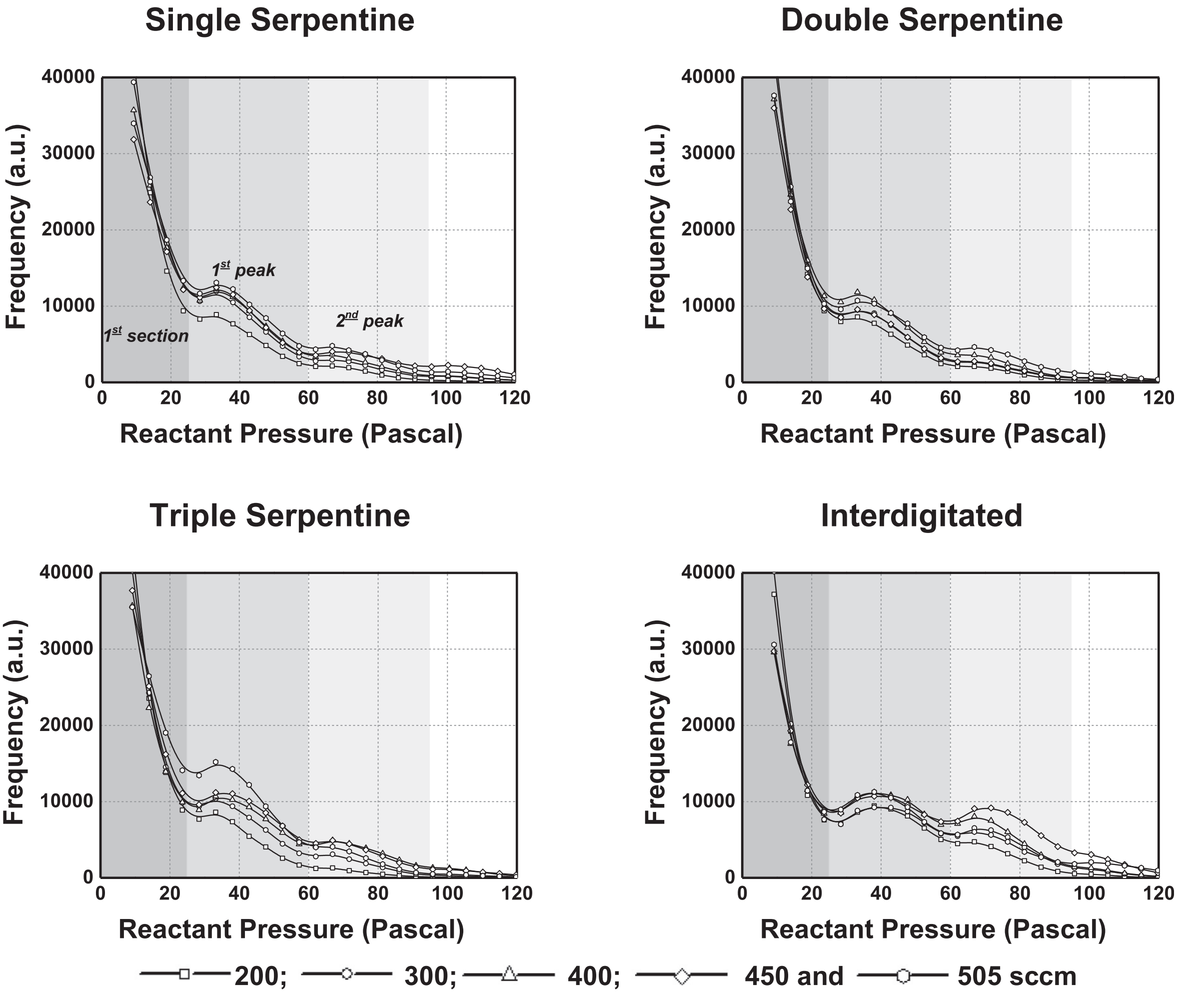

Fig. 5. Reactant partial pressure distributions as a function of flow field and flow rate obtained from analysis of the images in Fig. 2. 5 Pa bin width. A line plot rather than a bar plot is used to accentuate the peaks in the response.

also point to a clear contribution of convective flow towards expanding the catalyst layer utilization, i.e. fractional area covered by reactive gas, which is also noted for the S-type configuration, though at a reduced magnitude. This convective flow contributes to a greater total reactant partial pressure at the catalyst layer in comparison to the serpentine design, resulting in an improved PEFC performance (at the cost of a greater pressure drop), which has been experimentally seen by Souza et al. [77] and Zhang et al. [78]. It is noteworthy that Zhang et al. [78] have also observed that the ID flow field renders a more uniform current distribution than the S-type design, in every operating condition tested, which is in agreement with the results presented here (Fig. 2). This corroboration points to the importance of the channel design and to a proper understanding of reactant distribution towards limiting PEFC performance, where the present study contributes by decoupling the effect of liquid water, which is important for several experimental and modelling scenarios.

In an attempt to provide insights into the variation of local conditions for the different flow field design, the responses in Fig. 2 were totalled into bins, each 5 Pa wide from 0 to 120 Pa (see reference [22] for further details). Fig. 5 presents the reactant partial pressure distributions displayed in Fig. 2 for the entire flow rate range used. Despite the differences in reactant distribution seen in Fig. 2, it is seen that the designs share a somewhat similar profile, with a large fraction at values smaller than ≈ 25 Pa, and two distinguishable peaks between ≈ 25–60 and ≈ 60–95 Pa. The first peak is centred around 35 Pa for the S-type flow fields and at around 40 Pa for the ID design, while the second peak is centred around 70 Pa for every flow field design. The expected oxygen concentration distribution along a single **linear** channel of an operating fuel cell under conditions where the reaction is limited to electrokinetics are presented in the SI along with Figure S3. The comparison of data in Fig. 5 with the theoretical case (Figure S3) is most useful, although clearly the introduction of extra channels and the fact that the channels are not linear complicate the comparison. The lowest end of the theoretical plots is the expected outlet reactant partial pressure (matching the expectations from the stoichiometry of the reaction). The distribution along the channels in the theoretical case does not include any leaks and is a single monotonic function with discrete beginning and end values. In contrast, in the experimental case we have a distribution which includes peaks and which has reactant concentrations much lower than expected from the simple channel model, corresponding to areas of reactant starvation. Showing that there are regions of enhanced reactant concentration, and also regions of significantly reduced reactant concentration compared to the simple channel model. Although the general distribution fits the profile expected there are other areas of significant divergence.

The relative frequency for each section as a function of the flow rate is given in Fig. 6. Data in this graph points to a general trend: a decrease in the total relative frequency for the 0–25 Pa section with the inlet flow rate, with both first and second peaks showing an increase with the inlet flow rate, albeit the second peak corresponds only to a small fraction of the total count. It is noteworthy, though, to point out a distinction between the S-type and ID flow fields. Although only a small shift, the ID design shows a change in the trend for flow rates larger than 400 sccm, that is a decrease in total relative frequency for the two peaks, most notably the first one. The S-type designs, on the other hand, broadly maintain the same trend for the entire flow rate range studied; SS and TS also show a small decrease in total relative frequency for the 2nd peak for flow rate above 400–450 sccm and comparable increases in the first peak relative to the ID flow field.

Further analysing the binned data in Fig. 5 provides evidence that the intensity of the valleys between the sections/peaks (pointed out above) changes little with the flow rate, tending to stabilize at higher flow rates. A notable exception, possibly a statistical fluke, is the TS design for the valley at ≈ 25 Pa at a flow rate of 505 sccm. The conservation of such an aspect, along with the similar profile for all flow field designs, suggests well-defined processes for each section/peak. To gain further insights, each section/peak was analysed individually in the reactant partial pressure distributions. Fig. 7 exemplifies the analysis performed using the SS design for the flow rate range used in this work (for the remaining designs, please refer to the SI). The image data in Fig. 7 show that each section/peak presents distinct features in the reactant partial pressure distribution. The first section (0–25 Pa) mostly shows the contours of the SS channel and areas underneath the lands, corroborating the idea that the reactant crosses over between land sections (in accordance with the original interpretation given and discussed in [22]). The second section (1st peak, between 25 and 60 Pa) shows the main path taken by the reactant as it flows along the channel, and regions where cross over between channels are particularly intense. It is also noteworthy that this second section (1st peak) highlights the previously assigned convective transport effects [22], such as the spread of reactant after each turn of the channel, and the reduced partial pressure before each turn. Finally, the third section (2nd peak, between 60 and 95 Pa) illustrates similar features to the second section (1st peak), while strongly emphasizing the most prominent feature assigned to the convective transport [18,22], that is secondary flows leading to local maxima of reactant partial pressure at the second corner of each turn. It should be noted that there is some "mixing" between the assigned sections, of course, as the reactant partial pressure drops along the channel. However, these distinctions are clear at the beginning of the reactant pathway, maintaining its features for every flow rate values and flow fields analysed (see Figures S4 to S6).

Given the information presented above, an interpretation is proposed to the profiles seen in the binned data of Fig. 5. The second and third sections outlined (first and second peak in the distribution, respectively) correspond to convective transport due to the flow field design, with its peak intensity and centre being correlated with

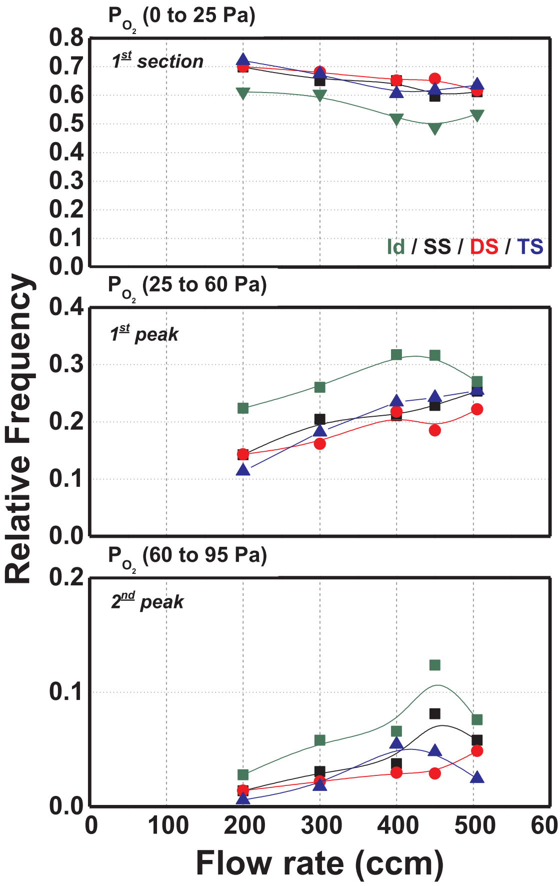

Fig. 6. Graphs represent the relative frequency of the reactant partial pressures for the three different sections given in Fig. 5.

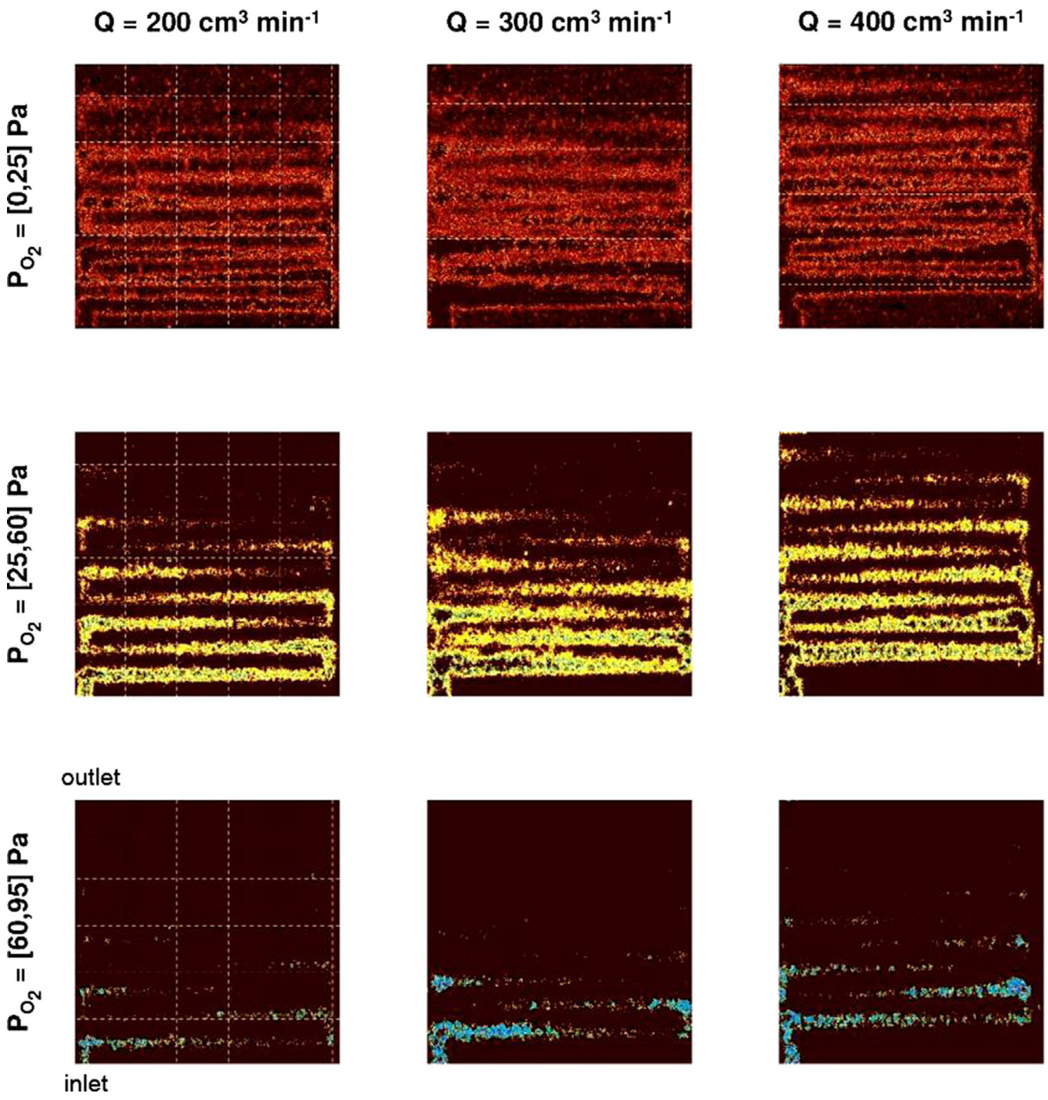

Fig. 7. Images representing oxygen (as ozone) partial pressure distributions in the catalyst layer of the pseudo-PEFC for the single serpentine flow field design (given in Fig. 3). The partial pressure distribution is divided into the three reactant partial pressure sections given in Fig. 5.

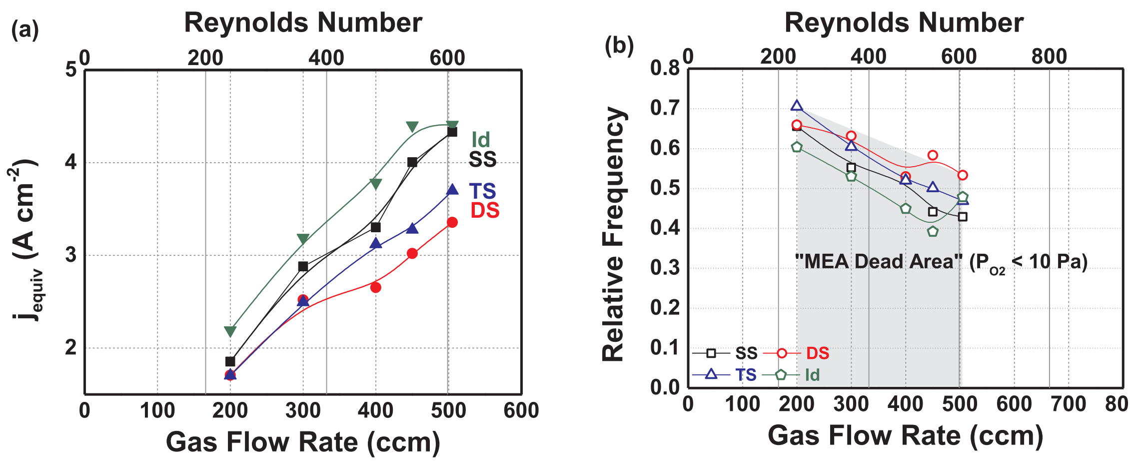

Fig. 8. (a) Graph illustrating the PEFC equivalent current density derived from the flow imaging results presented in Fig. 2. (b) Plots represent the relative frequency of areas of reactant partial pressures below 10 Pascal from Fig. 3. SS: single serpentine; DS: double serpentine; TS: triple serpentine; IS: interdigitated flow field designs. Other details given in Figure S1. Experimental details as per Fig. 5.

different processes of different magnitudes. In this way, it is expected that the total relative frequency of these sections should increase with the flow rate, as observed in Fig. 6. Additionally, a difference in magnitude suggests different dependencies on the flow rate, which is also observed, tentatively, in Fig. 6. Such higher order effects, so to speak, could be particularly dependent on the flow field design, highlighting the differences observed between the S-type and ID designs. Given that, the first section would be interpreted as resulting from the lack of convection, that is, mainly given by a diffusive transport at the edges of the reactant plumes. Using such interpretation, one can use the reactant partial pressure distributions in a more quantitative way in order to rationalize and study different flow field designs. For instance, the difference between the S-type and ID designs can now be assigned as due to the different contributions of convective transport. In the case of ID flow fields, it is expected that convection plays a major role in reactant distribution. This is shown by a large total relative frequency of sections two and three (Fig. 6), and a larger value of partial pressure around which the first peak is centred, relative to the S-type designs.

It should be noted, however, that further studies are necessary in order to validate the interpretation given here, and the utility of using such an approach. For instance, the studies performed here are mostly at low stoichiometric numbers as this helps accentuate the different aspects, but real fuel cells tend to operate at higher stoichiometries. Local modification in the flow fields, without altering the main design, such as the one pursued in the Toyota MIRAI fuel cell design, and investigated by Yoshizawa et al. [58] and Heidary et al. [59] could provide further clues to the interpretation of the peaks of the histograms and its origin. Additionally, improved spatial resolution and time-resolved experiments might enable the characterization of spatial and temporal scales, enabling further understanding of the underlying processes and full exploitation of this approach to improve flow field designs. Increased variability in flow field designs and a higher number of replicates are also important to validate the provided tool and to minimize artefacts.

Fig. 8 presents the equivalent current density of a PEFC, based on the integrated reactant partial pressure of each surface of Fig. 2. The equivalent current density is calculated based on the assumption of a FC operating at the same air flow rate and oxygen usage as seen for the ozone case. Under these conditions, we can calculate the rate of consumption of oxygen equivalent to ozone, R_{O_2}, which would give the same reactant distribution:

$$R_{O_2} = \frac{Q\%V_{O_2}}{\lambda_{O_3}\bar{V}_{O_2}} \tag{1}$$

Q is the inlet flow rate of gas, $\%V_{O_2}$ is the volume fraction of oxygen in dry air (≈ 0.21), and $\bar{V}_{O_2}$ is the molar volume of oxygen under the present experimental conditions. The ozone stoichiometry, λ_{O_3}, is obtained from the actual experiments, and is calculated by:

$$\lambda_{O_3} = \frac{J_{O_3}}{R_{O_3}} \tag{2}$$

where J_{O_3} is the inlet molar flux of ozone, while R_{O_3} is the rate of consumption, obtained from the difference between the inlet and outlet ozone concentrations. Using these equations, R_{O_2} can then be converted to current density using Faraday's law:

$$j = \frac{nFR_{O_2}}{A} \tag{3}$$

where $n = 4$ is the number of electrons exchanged in the oxygen reduction reaction, F is the Faraday constant, and A is the electrode geometric area.

These results suggest that among the S-type designs, the SS flow field would promote a higher total PEFC performance, whereas the ID design would result in an even higher total current density than the SS. Results in Fig. 8 are in the absence of water transport issues within the catalyst layer [22]. This fact could be interesting to decouple the effects of reactant and water mass transport. Upon comparing single and multichannel S-type designs, Liu et al. [74] have shown that the PEFC performance decreases with the number of channels, where the SS design presents a higher overall cell performance. Upon comparing SS and ID flow field designs, Souza et al. [77], Zhang et al. [78] and Hsieh et al. [79] have shown that the latter design results in a higher PEFC performance than the former. Results presented in Fig. 8 corroborates the cited literature, where SS flow field promotes a higher PEFC performance than DS and TS designs, while ID flow fields promote the highest current densities, which is inversely related to the area of the MEA not covered by reactant (dead area). This points to a major importance of reactant partial pressure magnitude and distribution to the overall PEFC performance, where results in Fig. 8 suggests that the flux of reactant across the catalyst layer area is primarily dictated by the flow field design. At corners, our results corroborate the water distribution measurements within both channel and land/rib areas of in operando PEFCs by Spendelow et al. [61] and Kowal et al. [62] through neutron imaging, and by Hartnig et al. [63] through synchrotron X-ray radiography. These works have found the amount of water to be higher in the land/rib regions in comparison to the channel regions. Based on the images in Fig. 2 and on the literature, water would accumulate in "reactant dead regions", that is, the regions described by the first section in Figs. 5 and 6 (0–10 Pa), meaning that transport is mainly governed by diffusion, and in the case of liquid water, capillarity. This corroboration would suggest that upon tackling reactant distribution, the transport of water would be significantly improved, as suggested by Yoshida and Kojima on the performance improvements of the stack of the Toyota MIRAI [17]. This information strongly suggests that the present reactant imaging technique may greatly promote the development of better FCs, both in terms of performance and durability, apart from being a unique tool for validating computational models.

5. Conclusions

Different imaging techniques were used to analyse the reactant distribution of a polymer electrolyte fuel cell (PEFC) with a single-channel serpentine flow field design, providing insights into its impact on in operando temperature distribution and post operando water build-up and membrane-electrode assembly (MEA) degradation. The results shown point out the correlation between reactant distribution, and temperature and water build-up distributions, strongly suggesting that properly engineered reactant distribution, as well as further studying it, directly helps with common issues in practical devices, i.e. heat and water management and device durability.

The reactant distribution, as a consequence of fluid flow, was probed using an optical imaging method that directly images the reaction rate at the cathodic catalyst layer of a prototype PEFC. The measured reaction rate is easily mapped to local reactant partial pressure, thus providing a powerful and easy-to-use tool to study reactant distribution in PEFC devices. When coupled to computational models, not only it provides strong constraints for validation, it also allows the inference of the actual flow field and contributions to reactant fluxes, providing in-depth, spatially resolved data on the device's reactant distribution throughout its components.

The temperature distribution was measured in situ and in operando, using thermocouples directly in contact with the porous transport layers (PTLs) in both cathode and anode, throughout the flow channels. Given the settings, it was possible to provide evidence that the secondary flows inferred from the reactant imaging technique are not artefacts, and do exist in an in operando PEFC, strongly contributing to heat management and hence the temperature distribution.

Water build-up was obtained from neutron tomography data, for a post operando carbon-based MEA. The build-up of water is linked to substrate and catalyst oxidation, which increases its hydrophilicity, thus providing a map to MEA degradation. The observed patterns neatly match the observed reactant, and thus reaction rate, distribution, suggesting increased local current densities contribute to MEA degradation. Consequently, non-uniform current density distribution leads to non-uniform water build-up and MEA degradation, once again highlight the importance of proper reactant distribution in a practical PEFC device.

Taken together, the correlations between the different techniques employed further improves understanding of reactant distribution within commonly used flow field designs. The results show that the single serpentine (SS) has the highest performance, among serpentine-type (S-type) designs, in terms of reactant distribution and equivalent current density, due to a large contribution of convective flow in the porous media. On the other hand, it underperforms compared to the interdigitated (ID) design, which presents the highest equivalent current density, however with a reactant distribution that seems to have a negative contribution of convection, i.e. with a large fraction of reactant dead areas" in the highest flow rate value. When considering the insights brought from the other techniques, these results imply that while the ID design is superior in terms of equivalent current density, it is likely to present a higher degradation rate in the MEA, as a result of the high, localized discontinuity in reaction rates. At the same time, the reactant distribution and the observed contribution of convection might lead to non-uniform temperature distributions, as the flow field is virtually confined to the regions bridging the inlet and outlet channels, failing to provide assistance in removing excess heat.

In summary, the results highlight the need to carefully consider additional variables when choosing, or developing, flow field designs, and that a compromise between performance and durability might be needed. The coupling of thoroughly established techniques with a new and versatile tool displayed in this work, can pave the way to minimize such trade backs in the quest for efficient and durable practical PEFC devices.

Acknowledgements

The authors would like to gratefully thank the U.K. Engineering and Physical Sciences research council under the Supergen Consortium, [grant number EP/G030995/1], and under the following grants EP/I014640/1 and EP/K503381/1 for financial assistance. T.L., I.K and OB are thankful to the Sao Paulo Research Foundation, FAPESP scholarships [grants number 2017/15304-6, 2016/12397-0 and 2013/11316-9 respectively]. Authors also acknowledge the support of FAPESP [grants number 2014/22130-6, 2014/09087-4 and 2017/11937-4], the RCGI Research Centre for Gas Innovation, sponsored by FAPESP [grant number 2014/50279-4].

Appendix A. Supplementary material

Supplementary data to this article can be found online at https://doi.org/10.1016/j.apenergy.2019.113421. The data used to produce the figures in this paper may be obatined by contacting the corresponding authors.

References

[1] Wang J. Theory and practice of flow field designs for fuel cell scaling-up: a critical review. Appl Energy 2015;157:640–63.

[2] Baik KD, Seo IS. Metallic bipolar plate with a multi-hole structure in the rib regions for polymer electrolyte membrane fuel cells. Appl Energy 2018;212:333–9.

[3] Huo S, Cooper NJ, Smith TL, Park JW, Jiao K. Experimental investigation on PEM fuel cell cold start behavior containing porous metal foam as cathode flow distributor. Appl Energy 2017;203:101–14.

[4] Li W, Zhang Q, Wang C, Yan X, Shen S, Xia G, et al. Experimental and numerical analysis of a three-dimensional flow field for PEMFCs. Appl Energy 2017;195:278–88.

[5] Borup R, Meyers J, Pivovar B, Kim YS, Mukundan R, Garland N, et al. Scientific aspects of polymer electrolyte fuel cell durability and degradation. Chem Rev 2007;107:3904–51.

[6] Ashrafi M, Shams M. The effects of flow-field orientation on water management in PEM fuel cells with serpentine channels. Appl Energy 2017;208:1083–96.

[7] Lemmon JP. Energy: reimagine fuel cells. Nature 2015;525:447–9.

[8] Armstrong RC, Wolfram C, de Jong KP, Gross R, Lewis NS, Boardman B, et al. The frontiers of energy. Nature Energy 2016;1:15020.

[9] Lee K-S, Spendelow JS, Choe Y-K, Fujimoto C, Kim YS. An operationally flexible fuel cell based on quaternary ammonium-biphosphate ion pairs. Nat Energy 2016;1:16120.

[10] Singdeo D, Dey T, Gaikwad S, Andreasen SJ, Ghosh PC. A new modified-serpentine flow field for application in high temperature polymer electrolyte fuel cell. Appl Energy 2017;195:13–22.

[11] Wang J. Barriers of scaling-up fuel cells: cost, durability and reliability. Energy 2015;80:509–21.

[12] Wang J, Wang H. Discrete approach for flow field designs of parallel channel configurations in fuel cells. Int J Hydrogen Energy 2012;37:10881–97.

[13] Wang J, Wang H. Flow-field designs of bipolar plates in PEM fuel cells: theory and applications. Fuel Cells 2012;12:989–1003.

[14] Watkins DS, Dircks KW, Epp DG. Novel fuel cell fluid flow field plate. Google Patents; 1991.

[15] Watkins DS, Dircks KW, Epp DG. Fuel cell fluid flow field plate. Google Patents; 1992.

[16] Dey T, Singdeo D, Basu RN, Bose M, Ghosh PC. Improvement in solid oxide fuel cell performance through design modifications: an approach based on root cause analysis. Int J Hydrogen Energy 2014;39:17258–66.

[17] Yoshida T, Kojima K. Toyota MIRAI fuel cell vehicle and progress toward a future hydrogen society. Electrochem. Soc. Interface 2015;24:45–9.

[18] Beruski O, Lopes T, Kucernak ARJ, Perez J. Investigation of convective transport in the gas diffusion layer used in polymer electrolyte fuel cells. Phys Rev Fluids 2017;2:103501.

[19] Wang C-Y. Fundamental models for fuel cell engineering. Chem Rev 2004;104:4727–66.

[20] Wang H, Yuan X-Z, Li HPEM. Fuel Cell Diagnostic Tools. CRC Press; 2011.

[21] Inukai J, Miyatake K, Takada K, Watanabe M, Hyakutake T, Nishide H, et al. Direct visualization of oxygen distribution in operating fuel cells. Angew Chem Int Ed 2008;47:2792–5.

[22] Lopes T, Ho M, Kakati BK, Kucernak ARJ. Assessing the performance of reactant transport layers and flow fields towards oxygen transport: a new imaging method based on chemiluminescence. J Power Sources 2015;274:382–92.

[23] Hakenjos A, Hebling C. Spatially resolved measurement of PEM fuel cells. J Power Sources 2005;145:307–11.

[24] Hakenjos A, Muenter H, Wittstadt U, Hebling C. A PEM fuel cell for combined measurement of current and temperature distribution, and flow field flooding. J Power Sources 2004;131:213–6.

[25] Robinson BJ, Shearing RP, Brett JD. Thermal imaging of electrochemical power systems: a review. J. Imag 2016;2.

[26] Lee S-K, Ito K, Ohshima T, Noda S, Sasaki K. In situ measurement of temperature distribution across a proton exchange membrane fuel cell. Electrochem Solid-State Lett 2009;12:B126–30.

[27] Matian M, Marquis A, Brett D, Brandon N. An experimentally validated heat transfer model for thermal management design in polymer electrolyte membrane fuel cells. Proc Instit Mech Eng A: J Power Energy. 2010;224:1069–81.

[28] Manthanwar AM, Lopes T, Atkins S, Kucernak A, Pistikopoulos EN. Functional characterization of polymer electrolyte fuel cell: in-situ experimental technique for spatiotemporally resolved temperature distribution [submitted for publication].

[29] Weber AZ, Borup RL, Darling RM, Das PK, Dursch TJ, Gu W, et al. A critical review of modeling transport phenomena in polymer-electrolyte fuel cells. J Electrochem Soc 2014;161:F1254–99.

[30] Manke I, Hartnig C, Grünerbel M, Lehnert W, Kardjilov N, Haibel A, et al. Investigation of water evolution and transport in fuel cells with high resolution synchrotron x-ray radiography. Appl Phys Lett 2007;90:174105.

[31] Markötter H, Alink R, Haußmann J, Dittmann K, Arlt T, Wieder F, et al. Visualization of the water distribution in perforated gas diffusion layers by means of synchrotron X-ray radiography. Int J Hydrogen Energy 2012;37:7757–61.

[32] Sinha PK, Halleck P, Wang C-Y. Quantification of liquid water saturation in a PEM fuel cell diffusion medium using X-ray Microtomography. Electrochem Solid-State Lett 2006;9:A344–8.

[33] Tsushima S, Teranishi K, Hirai S. Magnetic resonance imaging of the water distribution within a polymer electrolyte membrane in fuel cells. Electrochem Solid-State Lett 2004;7:A269–72.

[34] Tsushima S, Hirai S. Magnetic resonance imaging of water in operating polymer electrolyte membrane fuel cells. Fuel Cells 2009;9:506–17.

[35] Mosdale R, Gebel G, Pineri M. Water profile determination in a running proton exchange membrane fuel cell using small-angle neutron scattering. J Membr Sci 1996;118:269–77.

[36] Kramer D, Lehmann E, Frei G, Vontobel P, Wokaun A, Scherer GG. An on-line study of fuel cell behavior by thermal neutrons. Nucl Instrum Methods Phys Res Sect A 2005;542:52–60.

[37] Kramer D, Zhang J, Shimoi R, Lehmann E, Wokaun A, Shinohara K, et al. situ diagnostic of two-phase flow phenomena in polymer electrolyte fuel cells by neutron imaging: Part A. Experimental, data treatment, and quantification. Electrochim Acta 2005;50:2603–14.

[38] Bellows RJ, Lin MY, Arif M, Thompson AK, Jacobson D. Neutron imaging technique for in situ measurement of water transport gradients within nafion in polymer electrolyte fuel cells. J Electrochem Soc 1999;146:1099–103.

[39] Satija R, Jacobson DL, Arif M, Werner SA. In situ neutron imaging technique for evaluation of water management systems in operating PEM fuel cells. J Power Sources 2004;129:238–45.

[40] Mittal VO, Kunz HR, Fenton JM. Effect of catalyst properties on membrane

degradation rate and the underlying degradation mechanism in PEMFCs. J Electrochem Soc 2006;153:A1755–9.
[41] Yu J, Matsuura T, Yoshikawa Y, Islam MN, Hori M. In situ analysis of performance degradation of a PEMFC under nonsaturated humidification. Electrochem Solid-State Lett 2005;8:A156–8.
[42] Inaba M, Kinumoto T, Kiriake M, Umebayashi R, Tasaka A, Ogumi Z. Gas crossover and membrane degradation in polymer electrolyte fuel cells. Electrochim Acta 2006;51:5746–53.
[43] Ermel M, Oswald R, Mayer JC, Moravek A, Song G, Beck M, et al. Preparation methods to optimize the performance of sensor discs for fast chemiluminescence ozone analyzers. Environ Sci Technol 2013;47:1930–6.
[44] Malko D, Kucernak A, Lopes T. In-situ electrochemical quantification of active sites in Fe-N/C non-precious metal catalysts. Nat Commun 2016;7:13285.
[45] Lopes T, Kucernak A, Malko D, Ticianelli EA. mechanistic insights into the oxygen reduction reaction on metal–N–C electrocatalysts under fuel cell conditions. ChemElectroChem 2016;3:1580–90.
[46] Malko D, Lopes T, Ticianelli EA, Kucernak A. A catalyst layer optimisation approach using electrochemical impedance spectroscopy for PEM fuel cells operated with pyrolysed transition metal-N-C catalysts. J Power Sources 2016;323:189–200.
[47] Malko D, Lopes T, Symianakis E, Kucernak AR. The intriguing poison tolerance of non-precious metal oxygen reduction reaction (ORR) catalysts. J Mater Chem A 2016;4:142–52.
[48] Rakness K, Gordon G, Langlais B, Masschelein W, Matsumoto N, Richard Y, et al. Guideline for measurement of ozone concentration in the process gas from an ozone generator. Ozone Sci Eng 1996;18:209–29.
[49] Image IiaPDJIPPIbN. ImageJ is a Public Domain Java Image Processing Program Inspired by NIH Image, < http://rsb.info.nih.gov/ij/index/html. http://rsb.info.nih.gov/ij/index/html > [accessed on 21–03–2016].
[50] Schoueri RM, Domienikan C, de Toledo F, Andrade MLG, Stanojev Pereira MA, Pugliesi R. The new facility for neutron tomography of IPEN-CNEN/SP and its potential to investigate hydrogenous substances. Appl Radiat Isot 2014;84:22–6.
[51] Pereira MAS, Schoueri R, Domienikan C, Toledo Fd, Andrade MLG, Pugliesi R. The neutron tomography facility of IPEN-CNEN/SP and its potential to investigate ceramic objects from the Brazilian cultural heritage. Appl Radiat Isot 2013;75:6–10.
[52] Liu Z, Mao Z, Wu B, Wang L, Schmidt VM. Current density distribution in PEFC. J Power Sources 2005;141:205–10.
[53] Wilkinson M, Blanco M, Gu E, Martin JJ, Wilkinson DP, Zhang JJ, et al. In situ experimental technique for measurement of temperature and current distribution in proton exchange membrane fuel cells. Electrochem Solid-State Lett 2006;9:A507–11.
[54] Mench MM, Wang CY, Ishikawa M. In situ current distribution measurements in polymer electrolyte fuel cells. J Electrochem Soc 2003;150:A1052–9.
[55] Kulikovsky AA, Kucemak A, Kornyshev AA. Feeding PEM fuel cells. Electrochim Acta 2005;50:1323–33.
[56] Yang X-G, Burke N, Wang C-Y, Tajiri K, Shinohara K. Simultaneous measurements of species and current distributions in a PEFC under low-humidity operation. J Electrochem Soc 2005;152:A759–66.
[57] Kalyvas C, Kucernak A, Brett D, Hinds G, Atkins S, Brandon N. Spatially resolved diagnostic methods for polymer electrolyte fuel cells: a review. Wiley Interdiscipl Rev: Energy Environ 2014;3:254–75.
[58] Yoshizawa K, Ikezoe K, Tasaki Y, Kramer D, Lehmann EH, Scherer GG. Analysis of gas diffusion layer and flow-field design in a PEMFC using neutron radiography. J Electrochem Soc 2008;155:B223–7.
[59] Heidary H, Kermani MJ, Dabir B. Influences of bipolar plate channel blockages on PEM fuel cell performances. Energy Convers Manage 2016;124:51–60.
[60] Barbir F. Chapter five – fuel cell operating conditions. PEM Fuel Cells. 2nd ed. Boston: Academic Press; 2013. p. 119–57.
[61] Spendelow J, Mukundan R, Davey J, Rockward T, Hussey DS, Jacobson D, et al. High resolution neutron radiography imaging of operating PEM fuel cells: effect of flow configuration and gravity on water distribution. ECS Trans 2008;16:1345–55.
[62] Kowal JJ, Turhan A, Heller K, Brenizer J, Mench MM. Liquid water storage, distribution, and removal from diffusion media in PEFCS. J Electrochem Soc 2006;153:A1971–8.
[63] Hartnig C, Manke I, Kuhn R, Kleinau S, Goebbels J, Banhart J. High-resolution in-plane investigation of the water evolution and transport in PEM fuel cells. J Power Sources 2009;188:468–74.
[64] Gasteiger HA, Kocha SS, Sompalli B, Wagner FT. Activity benchmarks and requirements for Pt, Pt-alloy, and non-Pt oxygen reduction catalysts for PEMFCs. Appl Catal B 2005;56:9–35.
[65] Wood DL, Borup RL. Durability Aspects of Gas-Diffusion and Microporous Layers. In: Büchi FN, Inaba M, Schmidt TJ, editors. Polymer Electrolyte Fuel Cell Durability. Springer, New York: New York, NY; 2009. p. 159–95.
[66] Takeuchi N, Fuller TF. Modeling and investigation of design factors and their impact on carbon corrosion of PEMFC electrodes. J Electrochem Soc 2008;155:B770–5.
[67] Young AP, Colbow V, Harvey D, Rogers E, Wessel S. A semi-empirical two step carbon corrosion reaction model in PEM fuel cells. J Electrochem Soc 2013;160:F381–8.
[68] Takanohashi K, Suga T, Uchida M, Ueda T, Nagumo Y, Inukai J, et al. Simultaneous visualization of oxygen partial pressure, current density, and water droplets in serpentine fuel cell during power generation for understanding reaction distributions. J Power Sources 2017;343:135–41.
[69] Malko D, Kucernak A, Lopes T. Performance of Fe–N/C oxygen reduction electrocatalysts toward NO_2^-, NO, and NH_2OH electroreduction: from fundamental insights into the active center to a new method for environmental nitrite destruction. J Am Chem Soc 2016;138:16056–68.
[70] Choi CH, Baldizzone C, Grote J-P, Schuppert AK, Jaouen F, Mayrhofer KJJ. Stability of Fe-N-C catalysts in acidic medium studied by operando spectroscopy. Angew Chem Int Ed 2015;54:12753–7.
[71] Sahraie NR, Kramm UI, Steinberg J, Zhang Y, Thomas A, Reier T, et al. Quantifying the density and utilization of active sites in non-precious metal oxygen electroreduction catalysts. Nat Commun 2015;6:8618.
[72] Limjeerajarus N, Charoen-amornkitt P. Effect of different flow field designs and number of channels on performance of a small PEFC. Int J Hydrogen Energy 2015;40:7144–58.
[73] Wang X-D, Duan Y-Y, Yan W-M, Peng X-F. Local transport phenomena and cell performance of PEM fuel cells with various serpentine flow field designs. J Power Sources 2008;175:397–407.
[74] Liu H, Li P, Juarez-Robles D, Wang K, Hernandez-Guerrero A. Experimental study and comparison of various designs of gas flow fields to PEM fuel cells and cell stack performance. Front Energy Res 2014.;2.
[75] Tabe Y, Kikuta K, Chikahisa T, Kozakai M. Basic evaluation of separator type specific phenomena of polymer electrolyte membrane fuel cell by the measurement of water condensation characteristics and current density distribution. J Power Sources 2009;193:416–24.
[76] Hwnag JJ, Chang WR, Peng RG, Chen PY, Su A. Experimental and numerical studies of local current mapping on a PEM fuel cell. Int J Hydrogen Energy 2008;33:5718–27.
[77] de Souza A, Gonzalez ER. Influence of the operational parameters on the performance of polymer electrolyte membrane fuel cells with different flow fields. J Solid State Electrochem 2003;7:651–7.
[78] Zhang G, Guo L, Ma B, Liu H. Comparison of current distributions in proton exchange membrane fuel cells with interdigitated and serpentine flow fields. J Power Sources 2009;188:213–9.
[79] Hsieh S-S, Her B-S, Huang Y-J. Effect of pressure drop in different flow fields on water accumulation and current distribution for a micro PEM fuel cell. Energy Convers Manage 2011;52:975–82.